Enhanced photocatalytic activity of Ag-CsPbBr$_3$/CN composite for broad spectrum photocatalytic degradation of cephalosporin antibiotics 7-ACA

Yanyan Zhao[a,b], Yongbo Wang[c], Xuhua Liang[b], Huanxian Shi[a], Cunjin Wang[a], Jun Fan[d,*], Xiaoyun Hu[e,*], Enzhou Liu[a]

[a] School of Chemical Engineering, Northwest University, Xi'an, 710069, PR China
[b] College of Biology Pharmacy and Food Engineering, Shangluo University, Shangluo 726000, PR China
[c] School of Food and Biological Engineering, Shaanxi University of Science & Technology, Xi'an, 710021, PR China
[d] College of Food Science and Engineering, Northwest University, Xi'an, 710069, PR China
[e] School of Physics, Northwest University, Xi'an, 710069, PR China

ARTICLE INFO

ABSTRACT

A visible-light-induced antibiotics degradation system based on a nano-Ag, CsPbBr$_3$ quantum dot (QDs) and bulk g-C$_3$N$_4$ (CN) ternary assembly (Ag-CsPbBr$_3$/CN) has been firstly constructed under an organic phase environment, oleylamine (OLA) and oleic acid (OA) were used as surfactants to stabilize the CsPbBr$_3$, L-cysteine was used to facilitate the interaction between nano-Ag, CsPbBr$_3$ and CN. The new ternary assembly of Ag-CsPbBr$_3$/CN composite was used to degrade 7-aminocephalosporanic acid (7-ACA) under visible light irradiation, and the 7%-Ag-CsPbBr$_3$/CN composite displayed the superior photocatalytic activity, approximately 92.79% of 7-ACA has been degraded to CO$_2$, H$_2$O and other small molecules at 140 min, which was approximately 1.49-folds, 1.56-folds, 3.01-folds and 11.43-folds higher than 9%-CsPbBr$_3$/CN, 7%-Ag/CN, pure CN and pure CsPbBr$_3$, respectively. A possible mechanism for 7-ACA degradation over Ag-CsPbBr$_3$/CN composite were proposed according to detailed measurements of adsorption test, Brunauer-Emmett-Teller (BET) measurement, UV–vis diffuse reflectance spectra (DRS), photoluminescence spectra (PL), transient photocurrent response and electrochemical impedance spectroscopy (EIS) measurement, and the enhanced photocatalytic activity of Ag-CsPbBr$_3$/CN composite could be attributed to the excellent adsorbability, the enhanced light-harvesting and reduced charge recombination, as well as the synergistic effects of nano-Ag and CsPbBr$_3$ co-loaded with CN. In addition, Holes (h$^+$) and hydroxyl radicals ($^{\cdot}$OH) played major roles, electronic (e$^-$) and superoxide radical ($^{\cdot}$O$_2$-) played minor roles based on the reactive-species-trapping experiments, the NBT transformation and the 7-hydroxycoumarin fluorescent experiments. Furthermore, a possible 7-ACA degradation pathway was investigated based on the Liquid Chromatography-Mass spectroscopy (LC-MS) experiment to better understand the degradation process. The present opens up a new insight for using CsPbBr$_3$ as photocatalyst to degrade antibiotics.

1. Introduction

7-ACA is a significant basic skeleton of cephalosporin antibiotics, play a major role in cephalosporin synthesis industry [1,2], the primary properties of 7-ACA and main cephalosporin antibiotics were shown in Table. S1. Cephalosporin antibiotics belong to the class of β-lactam antibiotics, has been excessive consumption over the years due to the broad-spectrum antimicrobial activity, lead to a series of unidentified environmental effects and probable damage to aquatic life [3–5]. Photocatalysis technology has been considered to be the most advanced environmental friendly alternative technique to removal of the 7-ACA

from wastewater due to its non-pollution, low energy consumption and cost-effective [6].

Recently, graphitic carbon nitride (CN) has benefits of stability against photochemical corrosion, notable visible light absorption (band gap = 2.73 eV) and nontoxicity, has been studied widely in photocatalysis [7,8]. Nevertheless, the rapid recombination rate of photogenerated electron-hole pairs still restricts its practical applications [9,10]. Modern chemistry aims to synthesize novel photocatalyst for more light harvesting, faster forward charge separation, and the outstanding photocatalytic activity [11,12]. To enhance the photocatalytic activity of CN, the introduction of different noble metals (Ag, Au, Pt,

etc.), non-metallic elements or semiconductors to overcome the imperfections have been suggested [13–16].

Recently, QDs have emerged as a choice to enhance the photocatalytic activity of CN. Compared to other traditional materials, QDs have a small dimensions ranging and large surface area, which could enlarge probability of the contaction with target products [17]. QDs could widen the response range towards light and improve light-harvesting performance of CN due to the size-dependent spectroscopic properties [18]. Also, the large surface-to-volume ratio and the quantum confinement in QDs enhance the surface amplitude of the holes and electrons observably [19]. The $CsPbBr_3$ QDs, as an inorganic perovskite QDs, have triggered great interest among researchers for their outstanding performance of high absorption coefficient, long carrier lifetime, narrow size distribution, as well as high photoluminescence quantum yield to serve as photocatalyst [20–22]. Xu et al. have synthesized a $CsPbBr_3$ QDs/graphene oxide composite for photocatalytic CO_2 reduction [23], Li et al. have designed a facial method for coating of TiO_2 shell on $CsPbBr_3$ NCs for solar energy conversion in aqueous solution [24], and Balakrishnan et al. have explored that Au-$CsPbBr_3$ hybrid architecture with good colloidal stability and enhanced light energy harvesting applicability, provide new opportunities to develop their photocatalytic activity [25]. Therefore, $CsPbBr_3$ incorporated into semiconductor not only improve the visible light harvesting but also benefit from the efficient charge separation.

As a famous noble metal, Ag has been widely studied for its potent surface plasmon resonance (SPR) effects, characteristic optical and physical properties [26–28]. The introduction of Ag onto semiconductor surfaces conduces to expanding the light-harvesting scope, enhancing the light-absorption intensity, as well as improving the charge separation efficiency [29].

In this contribution, the new ternary assembly of Ag-$CsPbBr_3$/CN composite with outstanding photocatalytic activity has been firstly synthesized by loading nano-Ag onto the surface of $CsPbBr_3$/CN composite. In this ternary system, the $CsPbBr_3$ as the electron mediator facilitate photo-induced electron transfer from CN to $CsPbBr_3$ and then from $CsPbBr_3$ to nano-Ag enhances the efficiency for 7-ACA degradation. The microstructures, morphologies, surface chemical composition and photocatalytic activity of the Ag-$CsPbBr_3$/CN composite were investigated in detail. The possible mechanism of the enhanced photocatalytic activity was investigated based on·OH,·O_2-, transient photocurrent response, and electrochemical impedance spectroscopy. This finding is anticipated to provide new opportunities for constructing high-efficienct photocatalyst by utilizing halide perovskite QDs as semiconductor in photocatalytic degradation antibiotics applications.

2. Experimental

2.1. Materials

$PbBr_2$, Cs_2CO_3, OLA, OA, 1-octadecene (ODE) and Nitrotetrazolium blue chloride (NBT) were acquired from Shanghai Macklin Biochemical Co. Ltd. Silver nitrate ($AgNO_3$) and L-cysteine were obtained from Guangzhou brilliance technology co., LTD. Melamine ($C_3H_6N_6$) and Hydrazine hydrate (H_6N_2O) were purchased from Shanghai Sinopharm Pharmaceutical Co., Ltd. Isopropanol (IPA), P-benzoquinone (BQ), Thylenediamine tetraacetic acid disodium salt (EDTA-2Na), Coumarin and Potassium dichromate ($K_2Cr_2O_7$) were purchased from Tianjin Fuyu Fine Chemical Co., Ltd. 7-ACA was procured from Aladdin Industrial Corporation.

2.2. Photocatalysts synthesis

2.2.1. Synthesis of the $CsPbBr_3$ and $CsPbBr_3$/CN composite

$CsPbBr_3$ was synthesized following a route published by Xu et al. with minor alterations [23]. In this experiment, ODE is used as the organic phase, OLA and OA are used as surfactants to stabilize the $CsPbBr_3$. Typically, the Cs-OA precursor solution was prepared by mixing Cs_2CO_3 (1.25 mmol) with ODE (20 mL) and OA (2 mL) solution in a 3-neck flask with nitrogen bubbling at 150℃ for 2 h. 0.61 mmol $PbBr_2$ were dissolved into 10 mL ODE, 1 mL OA and 1 mL OLA in another 3-neck flask and stirred for 30 min at 100℃ to obtain a clear solution. Subsequently 4 ml of Cs-OA precursor solution were added to this solution with nitrogen bubbling at 100℃ and refluxed for 30 min, the $CsPbBr_3$ were obtained after centrifuging and washing process (by methyl alcohol) twice. For fabrication of $CsPbBr_3$/CN composite, the ODE solution was substituted by the CN/ODE solution (The CN was synthesized according to our earlier report [3–5]), The collected precipitates were represented by x-$CsPbBr_3$/CN, where "x" represent mass ratio percentage of $CsPbBr_3$ and CN. For instance, 9%-$CsPbBr_3$/CN represent that 9 mg $CsPbBr_3$ were uniform distribution on the surface of 100 mg CN, the synthesis process was shown in Scheme. S1.

#### 2.2.2. Fabrication of Ag-$CsPbBr_3$/CN composite

As the optimal photocatalytic activity of 9%-$CsPbBr_3$/CN composite according to the photocatalytic experiments, the Ag-$CsPbBr_3$/CN composite was prepared to modify 9%-$CsPbBr_3$/CN composite with different mass fraction of nano-Ag, and the composite named as x-Ag-$CsPbBr_3$/CN, where x represent 3%, 5%, 7%, 9% and 11% nano-Ag in the Ag-$CsPbBr_3$/CN. The preparation process was as follows: 0.1 g of the as-prepared 9%-$CsPbBr_3$/CN composite was dissolved in 100 mL of 80% ethanol solution with 0.01 g L-cysteine, stir for 30 min to obtained the L-cysteine-$CsPbBr_3$/CN solution. Subsequently, The different volumes of Ag solution (0.1 g $AgNO_3$ and 2 mL Hydrazine hydrate were dispersed in 50 mL deionized water at 100℃ for reflu × 1 h) were added to the L-cysteine-$CsPbBr_3$/CN solution for stirring 3 h. Thereafter, the suspension was centrifuged, washed with ethanol solution several times, and dried in an oven at 60 °C for 20 h to obtain the x-Ag-$CsPbBr_3$/CN composite, The synthesis process was shown in Scheme 1. Ag/CN was synthesized by replacing $CsPbBr_3$/CN with pure CN.

2.3. Characterization

The Surface chemical composition of the as-prepared samples were investigated by Fourier transform infrared spectra (FTIR, Perkin Elmer Frontier FTIR with ATR accessory), X-ray diffraction (XRD, Shimadzu XRD-6000 powder diffractometer), and X-ray photoelectron spectroscopy (XPS, Kratos AXIS NOVA). The morphology and microstructure of the as-prepared samples were obtained via a field emission Transmission electron microscopy (TEM) and high-resolution TEM images (JEOL JEM-2100), Scanning electron microscopy (SEM, JSM-6390 A) with Elemental mapping and energy dispersive spectroscopy (EDS). Brunauer-Emmett-Teller (BET) surface areas of the as-prepared samples were investigated with quantachrome NOVA 2000e (USA) by N_2 adsorption-desorption isotherm. The UV-vis diffuse reflectance spectra were determined with a Shimadzu UV-3600 UV/vis/NIR spectrophotometer with $BaSO_4$ as a reflectance standard. Photoluminescence (PL) spectra were recorded with a florescence spectrophotometer (Hitachi F-7000).

2.4. Photocatalytic experiments and 7-ACA analysis

Photocatalytic experiments were performed under visible light with UV filter to block the UV light (300 W Xe lamp). In a typical procedure, 100 mL of a 7-ACA solution (10 mg mL^{-1}) and 100 mg as-prepared photocatalyst were mixed in a beaker and stirred in the dark for 70 min to acquire the adsorption-desorption equilibrium. The mixture was irradiated under visible light and 5 mL of the suspensions were withdrawn and centrifuged at given intervals. The absorbance of 7-ACA were determined by using high performance liquid chromatography (HPLC, Shimadzu LC-20 A) with a ultraviolet detector and a C_{18} column (particle size 5 μm, 4.6 × 250 mm). The mobile phase consisted of 90% sodium acetate-acetic acid buffer solution (pH = 4.75) and 10%
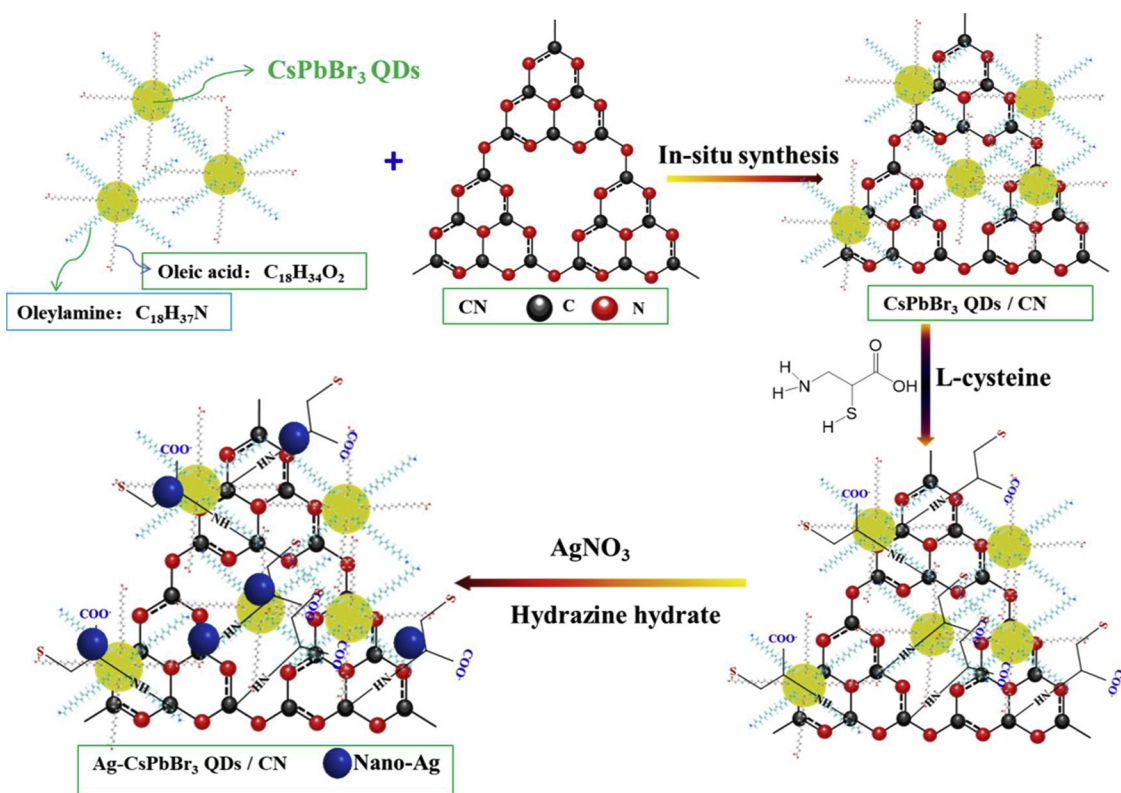
Scheme 1. Synthetic process of the Ag-CsPbBr₃/CN ternary assembly (not to scale).

acetonitrile at a flow rate of 1.0 mL/min. The injection volume was 10 μL. The degradation rate is calculated by Eq. (1). Where C_0 is the initial concentration and C_t is the reaction concentration, respectively.

$$\text{Photodegradation rate} = (1 - C_t/C_0) \times 100\% \tag{1}$$

2.5. Intermediates test

The intermediates were determined through a LC-MS spectroscopy (Shimadzu, PR-LCMS-2020) experiment composed of C_{18} column (particle size 5 μm, 4.6 × 250 mm). The mobile phase consisted of 90% formic acid solution (0.1% acid solution in deionized water) and 10% acetonitrile at a flow rate of 1.0 mL/min, the injection volume was 20 μL. The samples were scanned in electron spray positive (ES+) ion mode.

2.6. Detection of reactive species

For the indirect analysis of the reactive species, the radical scavenging experiments were carried out by adding IPA for hydroxyl radical (˙OH), BQ for superoxide radical (˙O_2^-), $K_2Cr_2O_7$ for electrons (e-) and EDTA-2Na for holes (h⁺) quencher during the 7-ACA photocatalytic degradation process, and the degradation rate was calculated as Eq. (1).

2.7. Evaluation of ˙O_2^- and ˙OH

NBT method was employed to further evaluate the ˙O_2^- radicals. About 10 mg of the as-prepared samples was mixed with NBT solution (5 × 10⁻⁵ mol·L⁻¹, 100 mL) under visible light irradiation (300 W Xe lamp, λ ≥ 420 nm), and the amount of ˙O_2^- radicals was quantitatively analyzed with a UV-3600 spectrophotometer at 259 nm after centrifugation.

A 7-hydroxycoumarin photoluminescence technique was carried out

to further evaluate the ˙OH radicals. 20 mg of the as-prepared samples were suspended into the coumarin solution (0.001 mol·L⁻¹, 30 mL) under constant stirring. The solution was irradiated under visible light (300 W Xe lamp, λ ≥ 420 nm) and 5 mL of the suspension liquid was taken out at intervals of 30 min, then centrifuged to obtain the supernatant. The supernatant including 7-hydroxycoumarin was measured with the PL spectra at excitation wavelength of 390 nm and emission wavelength of 455 nm.

3. Results and discussion

3.1. Structure characteristics

3.1.1. Structure characteristics of CsPbBr₃ QDs

The as-prepared CsPbBr₃ in organic phase with a bright yellow colour at ambient light irradiation and a bright turquoise luorescence colour at UV light irradiation, and the CsPbBr₃ was luminous yellow power after centrifugation and dry at 60℃. The absorption and PL spectrum of the Liquid CsPbBr₃ were presented in Fig.1a. The maximum absorption wavelength of UV spectrum at 340 nm, and the PL spectrum revealed that the maximum emission wavelength were at 515 nm. The FTIR spectra, XRD pattern, and UV–vis diffused absorption spectra of the as-prepared power CsPbBr₃ were shown in Fig.1b-d. The signals at 2922 and 2857 cm⁻¹ in FTIR spectra were assigned to antisymmetric stretching vibration of −CH₃, the signal at 1719 cm⁻¹ could be attributed to the –C=O stretching vibration of OA, the FTIR results revealed that the OA, OLA and ODE were successfully modified on the surface of the CsPbBr₃ (Fig. 1b). As shown in Fig.1c, the signals at 15.2, 21.5, 26.3, 30.4, 30.7, 34.2, 37.6 and 43.7° could be attributed to the (100), (110), (111), (002), (200), (210), (211) and (202) cubic planes of the crystal structure of perovskite in accordance with JCPDS 18-0364 [24,25,30–32]. The optical absorption of CsPbBr₃ was investigated by using an UV-vis spectrometer, the absorbing boundary was at 556 nm, and the bandgap (Eg) of CsPbBr₃ was about 2.23 eV according to the equation of $E_g = 1240/\lambda$ (where λ is the absorbance boundary of the
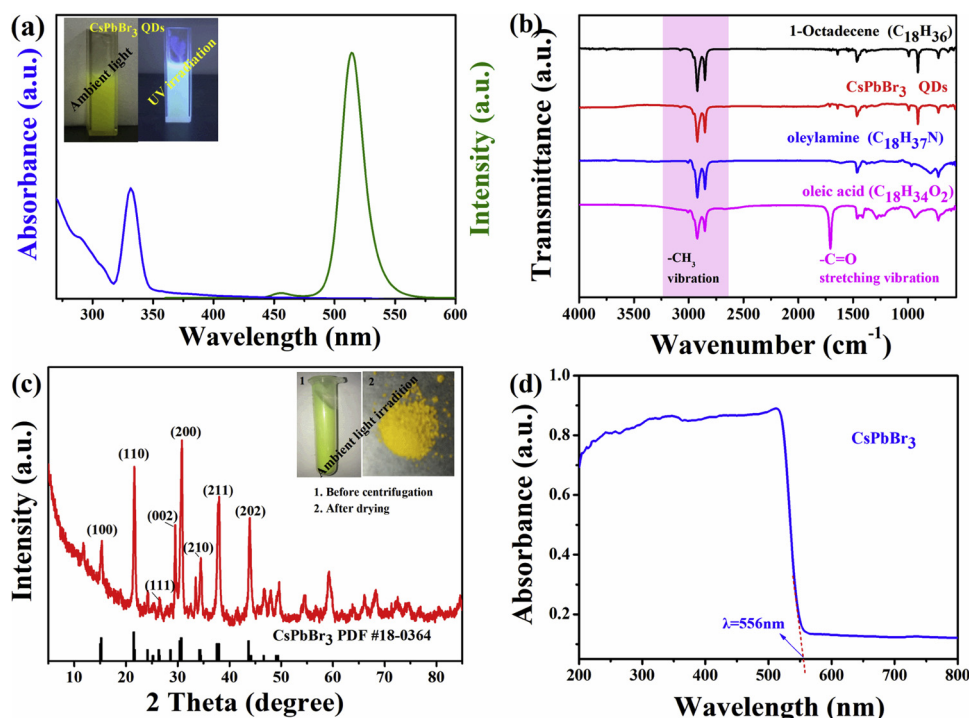
Fig. 1. (a) UV-vis and PL spectrum, (b) FTIR spectra, (c) XRD pattern, and (d) UV–vis diffused absorption spectra of the CsPbBr$_3$.

sample), the result was identical with those reported in literature [30,33,34].

3.1.2. Surface chemical composition and morphology analysis

The FTIR spectra of the as-prepared samples were shown in Fig. 2a, and the characteristic absorption band for -CH$_3$ antisymmetric stretching vibration at 2922 and 2857 cm^{-1} could be found on the surface of CsPbBr$_3$ QDs, 7%-CsPbBr$_3$/CN, and 9%-Ag-CsPbBr$_3$/CN samples, the signals at 808 cm^{-1} could be attributed to the vibration

mode of s-triazine unit and the several vibration bands at 1000-1800 cm^{-1} region were assigned to the C−N or C═N group of CN semiconductor [35,36]. The FTIR spectra results indicated the successful structure of the CsPbBr$_3$/CN and Ag-CsPbBr$_3$/CN composite.

The XRD patterns, energy dispersive spectroscopy (EDS) and elemental mapping were employed to better understand the structures of the as-prepared samples. As shown in Fig. 2b, The characteristic diffraction peaks at 13.0 and 27.2° can be indexed to the (100) and (002) diffraction plane of CN (JCPDS 87-1526) [3–5], the signals at 15.2,
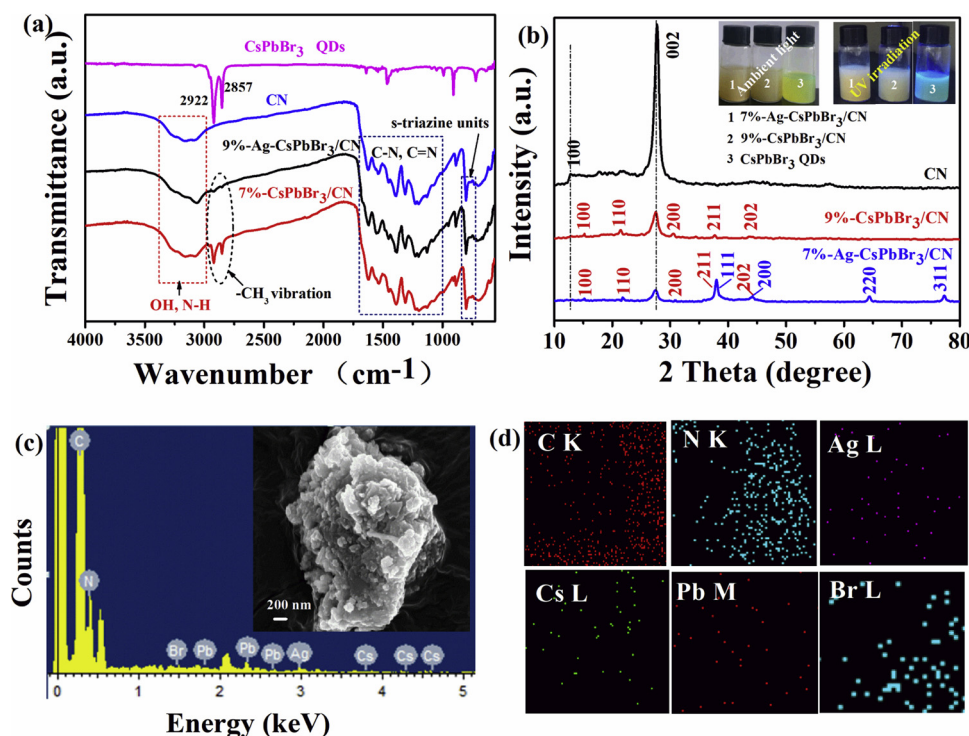

Fig. 2. (a) FTIR spectra, (b) XRD pattern of the as-prepared samples. (c) SEM image and EDS spectrum, (d) Elemental mapping of Ag- CsPbBr$_3$/CN sample.
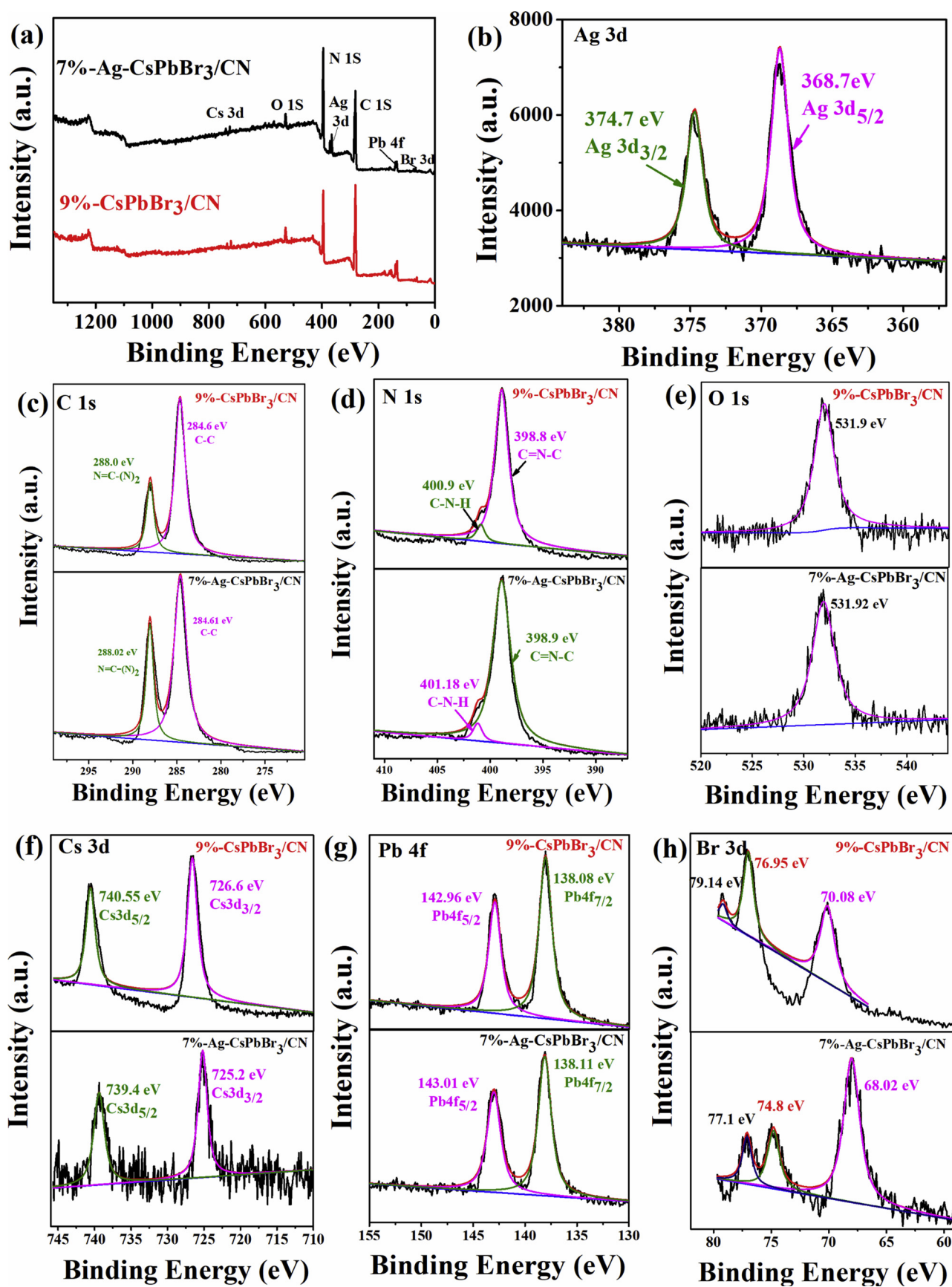
Fig. 3. XPS spectra of Ag-CsPbBr$_3$/CN and CsPbBr$_3$/CN composite, (a) full-scan spectra, high-resolution XPS spectra of (b) Ag 3d, (c) C 1 s, (d) N 1 s, (e) O 1 s, (f) Cs 3d, (g) Pb 4f, and (h) Br 3d.

21.5, 30.6, 37.6 and 43.6° corresponded to the (100), (110), (200), (211) and (202) cubic planes of the crystal structure of $CsPbBr_3$. For the 9%-Ag-CsPbBr$_3$/CN composite, the signals at 38.2, 44.2° were too close to the signals at 37.6 and 43.6° to distinguish, and the two additional signals at 64.4 and 77.4° indexed to the (220), and (311) planes of the cubic crystal phase of Ag (JCPDS65-2871) [37,38]. The 9%-CsPbBr$_3$/CN and 7%-Ag-CsPbBr$_3$/CN composite exhibit the same tawny colour at ambient light and UV light irradiation in Fig. 2a inset. The EDS results in Fig. 2c and the elemental mapping results in Fig. 2d reveals that C, N, Br, Pb, Cs and Ag elements were present in 7%-Ag-CsPbBr$_3$/CN composite, confirming that $CsPbBr_3$ and nano-Ag were successfully modified on the surface of CN. The SEM images of 7%-Ag-CsPbBr$_3$/CN composite in Fig. 2c inset shows irregular bulk shape mainly because the bulk structure of pure CN.

Furthermore, XPS characterizations were performed to characterize the surface chemical composition. The full-scan spectra revealed that C, N, Br, Pb, Cs and O elements co-exist in the $CsPbBr_3$/CN composite, it could be observed that Ag-CsPbBr$_3$/CN composite also contained Ag element (Fig. 3a). The high-resolution plots in Fig. 3b demonstrates that two characteristic peaks of Ag centered at 368.7 and 374.7 eV correspond to Ag $3d_{5/2}$ and Ag $3d_{3/2}$ binding energies of nano-Ag for Ag-CsPbBr$_3$/CN composite [39]. The C 1s high-resolution XPS spectrum could be divided into two different peaks at 284.6 and 288.0 eV in $CsPbBr_3$/CN composite indicating C-C and N = C-(N)$_2$ (Fig. 3c) [40], the N 1s of $CsPbBr_3$/CN composite contain two peaks at 398.8 and 400.9 eV corresponding to C = N-C and N-(C)$_3$ in Fig. 3d [3–5,41], and the binding energies of C 1s and N 1s were no obvious change after introducing Ag. In addition, the O 1s at 531.9 eV in Fig. 3e were assigned to the organic ligands of OA on the surface of $CsPbBr_3$ QDs. The high-resolution XPS spectrums of Cs 3d, Pb 4f, and Br 3d in Fig. 3f-h indicates that their distinct binding energies were in keeping with the presented reports [23,24,42–44]. The XPS spectra of Cs $3d_{3/2}$ and Cs $3d_{5/2}$ located at 726.6 and 740.55 eV in $CsPbBr_3$/CN composite, and at 725.2 and 739.4 eV in Ag-CsPbBr$_3$/CN composite, respectively. The peaks at 138.08 and 142.96 eV in $CsPbBr_3$/CN composite, at 138.11 and 143.01 eV in Ag-CsPbBr$_3$/CN composite can be attributed to the Pb $4f_{7/2}$ and Pb $4f_{5/2}$. The binding energies of Br 3d appeared at 70.08, 76.95 and 79.14 eV in $CsPbBr_3$/CN composite, and at 68.02, 74.8 and 77.1 eV in Ag-CsPbBr$_3$/CN composite. The obvious change of Cs 3d, Pb 4f, and Br 3d signals could be attribute to the introduction of metal Ag.

The TEM and HRTEM images of $CsPbBr_3$ QDs were presented in Fig. 4a-c. The monodisperse $CsPbBr_3$ QDs had a fairy uniform size and an average diameter of 5-10 nm, a lattice spacing of 0.240 nm corresponding to the (211) plane, which revealed the $CsPbBr_3$ particles had a very good crystallinity [23]. As shown in Fig. 4d-f, the $CsPbBr_3$ QDs were evenly dispersed on the surface of the CN sample, the crystallinity and diameter of the $CsPbBr_3$ QDs remained identical, the lattice spacing was 0.239 nm. Fig. 4g-i displays the TEM and HRTEM images of Ag-CsPbBr$_3$/CN composite, the deep color observation shown in Fig. 4g-h suggests a considerable amount of $CsPbBr_3$ QDs and metal Ag on the surface of CN. The lattice spacings of 0.240, 0.239 and 0.146 nm respectively measured from Fig. 4i attributes to the crystal plane of $CsPbBr_3$ (211) plane and Ag (111) facet [45], indicating the successful preparation of Ag-CsPbBr$_3$/CN composite.

3.2. Evaluation of photocatalytic activity

3.2.1. Photocatalytic degradation of 7-ACA

7-ACA was degraded with the as-prepared samples under visible light irradiation to investigate the outstanding photocatalytic activity of the Ag-CsPbBr$_3$/CN composite. As shown Fig. 5a, the peak at retention time (RT) of 2.49 min was divided into two other peaks at RT of 1.24 and 1.92 min at the beginning of the photocatalytic degradation process, and the RT of 1.24 min can be attribute to the hydroxymethyl-7-amincephalic acid (D-7-ACA) because of the instability of 7-ACA. The intensity of all peaks weakening as the photocatalytic degradation time

was prolonged, suggesting that 7-ACA could be degraded. As shown in Fig. S1 and Fig. 5b, the 7-ACA degradation rate displayed inconspicuous change only under visible light irradiation, indicating the unimportant of self-photolysis. The degradation rate with pure $CsPbBr_3$ and pure CN were approximately 19.78 and 55.91%, respectively. The photocatalytic activity of Ag/CN, CsPbBr$_3$/CN and Ag-CsPbBr$_3$/CN composite were significantly improved, and the degradation rate with 7%-Ag/CN and 9%-CsPbBr$_3$/CN composite were about 79.12% and 84.45%, respectively. The 9%-CsPbBr$_3$/CN composite displayed the highest photocatalytic activity, suggesting the optimal proportion of $CsPbBr_3$ and CN. The 7-ACA degradation rate were dramatically enhanced after introduction of nano-Ag, 7%-Ag-CsPbBr$_3$/CN composite displayed the outstanding photocatalytic activity and the 7-ACA degradation rate was about 92.79%, indicating the critical role of $CsPbBr_3$ and Ag, as well as the synergetic catalytic effect between $CsPbBr_3$, Ag and CN for photocatalytic activity enhancement.

The pseudo-first-order model as expressed by Eq. (2) was used to describe the 7-ACA degradation kinetics. As shown in Fig. 5c, the plots of irradiation time (min) versus the Ln (C$_0$/C$_t$) displayed a nearly straight line, and the R^2 were 0.9915, 0.9927, 0.9978, 0.9895 and 0.9873 of pure CN, 9%-CsPbBr$_3$/CN, 7%-Ag-CsPbBr$_3$/CN, Ag/CN and CsPbBr$_3$, respectively.

$$- \text{Ln } (C_t/C_0) = kt \qquad (2)$$

Fig. 5d depicts the effects of different photocatalyst for 7-ACA degradation under visible light irradiation for 140 min, and the k_{obs} of 7%-Ag-CsPbBr$_3$/CN composite was 18.97×10^{-3} min^{-1}, which was approximately 1.49-folds, 1.56-folds, 3.01-folds and 11.43-folds higher than 9%-CsPbBr$_3$/CN, 7%-Ag/CN, pure CN and pure CsPbBr$_3$, respectively. The results corroborated that new ternary assembly of Ag-CsPbBr$_3$/CN composite with excellent photocatalytic activity, which have effective potential applications in removing cephalosporin antibiotic in the aquatic environment.

3.2.2. Possible degradation pathway of cephalosporin antibiotic 7-ACA

In order to better understand the photocatalytic degradation process of 7-ACA with Ag-CsPbBr$_3$/CN composite, the LC-MS experiments were performed based on the intermediates identification. Fig. S2 depicted the ion chromatographs and mass spectra of 7-ACA at 4.433, 5.249, 6.233, 6.882 and 7.049 min, respectively, and the possible degradation pathway of 7-ACA based on the ion chromatographs were shown in Fig. 6. The structure A protonated ion peak at m/z 272.05 could be attribute to 7-ACA, which can be degrade to structure B (D-7-ACA) at m/z 230.24 by loss of acetyl group. It is well known that ring-opening reactions of β-lactam antibiotics structure is easy to take place during the degradation process, the 7-ACA could be degrade to the structure C (m/z = 60.12) and structure D (m/z = 230.24) with the ring-opening reactions of β-lactam, and the structure D could be degrade to structure F (m/z = 60.12) as degradation time was prolong. The intermediate E (m/z 227) was observed due to the loss of –COOH group from 7-ACA. And with an extension of degradation time, all the intermediates could be degrade to CO_2, and H_2O. The LC-MS experiments also indicated the potential applications of Ag-CsPbBr$_3$/CN composite in removing cephalosporin antibiotic in the aquatic environment.

3.2.3. Photocatalytic degradation of ceftriaxone sodium and cefixime with 7%-Ag-CsPbBr$_3$/CN composite

In order to assess the photocatalytic applications of the Ag-CsPbBr$_3$/CN composite in degradation of other cephalosporin antibiotics, the degradation of cefixime and ceftriaxone sodium with 7%-Ag-CsPbBr$_3$/CN composite were performed under visible light irradiation, and the results are shown in Fig. 7. The absorbance of cefixime and ceftriaxone sodium decreased obviously along with the irradiation time increasing, indicating the degradation of cephalosporin antibiotics. The degradation rate of cefixime and ceftriaxone sodium were approximately
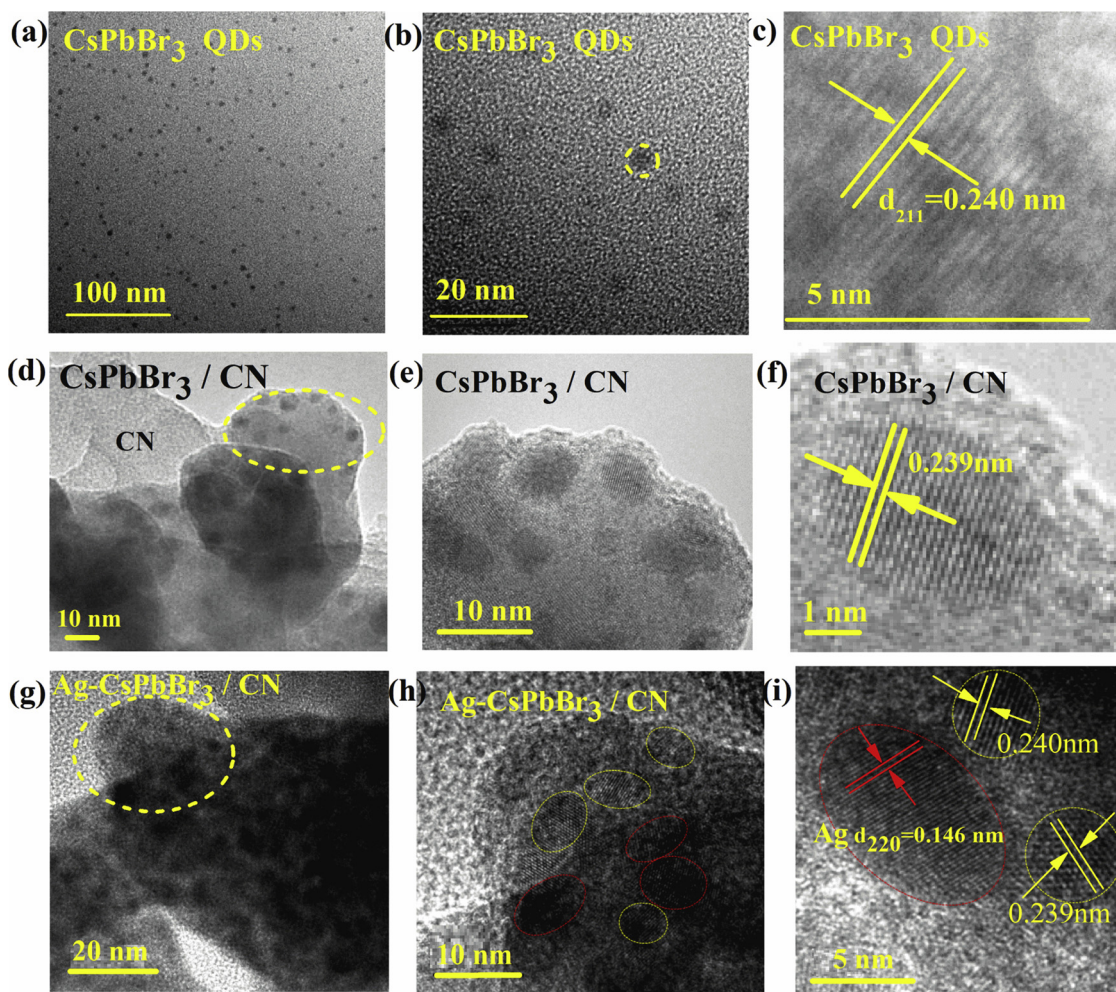
Fig. 4. TEM and HRTEM images of the as-prepared samples. (a-c) CsPbBr$_3$ QDs, (d-f) CsPbBr$_3$/CN composite, (g-i) Ag-CsPbBr$_3$/CN composite.

94.23% and 93.41% at 140 min, respectively, and the plots of irradiation time (min) versus the Ln(C$_0$/C$_t$) displayed a nearly straight line, illustrating the pseudo-first-order kinetics of cefixime and ceftriaxone sodium degradation process. The results indicated the effectively utilized of the Ag-CsPbBr$_3$/CN composite for the degradation of other cephalosporin antibiotics.

3.3. Enhanced photocatalytic activity of Ag-CsPbBr$_3$/CN composite

The enhanced photocatalytic activity of Ag-CsPbBr$_3$/CN composite could be attributed to the synergistic effects of nano-Ag and CsPbBr$_3$ co-loaded with CN. As our best knowledge, the excellent antibiotic adsorbability, expanding light-harvesting scope, as well as charge transportation and separation ability are three main factors restrict the photocatalytic activity of the composite [46]. Generally, the more adsorbed target molecules lead to the more chance for the photocatalytic reactions, therefore, the adsorption experiments were carried out to evaluation the adsorbability of the as-prepared samples, and the results displayed in Fig. 8a. The adsorbability of pure CN, 9%-CsPbBr$_3$/CN composite and 7%-Ag-CsPbBr$_3$/CN composite were rapidly increased before 20 min, then became closer to balance, and the 7%-Ag-CsPbBr$_3$/CN composite displayed the best adsorption ability.

Specific surface area play an important role in photocatalytic degradation process. Larger specific surface area, better adsorbability, and more active sites. Hence, N$_2$ adsorption-desorption isotherms were evaluated to measure the surface areas and the results were presented in Fig. 8b. The BET surface areas of 7%-Ag-CsPbBr$_3$/CN composite was

223.69 m^2/g, which was ca. 1.43 times higher than the 9%-CsPbBr$_3$/CN composite (156.73 m^2/g), and ca. 7.78 times higher than that of pure CN (28.76 m^2/g), suggesting introduction of nano-Ag and CsPbBr$_3$ QDs to the surface of pure CN could enhance the surface areas as well as provide more active sites for photocatalytic degradation of 7-ACA.

To clarify the role of Ag-CsPbBr$_3$/CN composite on enhancing the 7-ACA degradation rate, UV-vis diffuse reflectance spectra, PL spectra, transient photocurrent response, and EIS experiments were conducted. The UV–vis absorption spectra in Fig. 8c depicted that the UV–vis spectra of pure CN exhibited a visible absorption edge at 455 nm, which triggering by the electron transition from the VB populated by N 2p orbitals to the CB formed by hybridized C 2p and N 2p orbitals (π→π* transitions) [47,48]. The photo-responding range displayed an obvious red shift at 558 nm after loading CsPbBr$_3$ on to the surface of CN, indicating the CsPbBr$_3$ QDs could obviously expand the light-harvesting scope. The adsorption edge of 7%-Ag-CsPbBr$_3$/CN composite was 567 nm, leading to an extended response to visible light, suggesting more visible-light harvesting.

The charge transportation and separation ability of the as-prepared samples were revealed. The PL spectra of pure CN, 9%-CsPbBr$_3$/CN composite and 7%-Ag-CsPbBr$_3$/CN composite at an excitation wavelength of 345 nm were presented in Fig. 8d. The pure CN showed an intense fluorescence emission peak at ca. 452 nm, after introduction of CsPbBr$_3$ on to the CN, the PL intensity decreased significantly. It's clearly seen from Fig. 8d that the fluorescence emission peak of Ag-CsPbBr$_3$/CN composite shift blue, which may because the synergistic effects of nano-Ag and CsPbBr$_3$ co-loaded with CN. The Ag-CsPbBr$_3$/CN
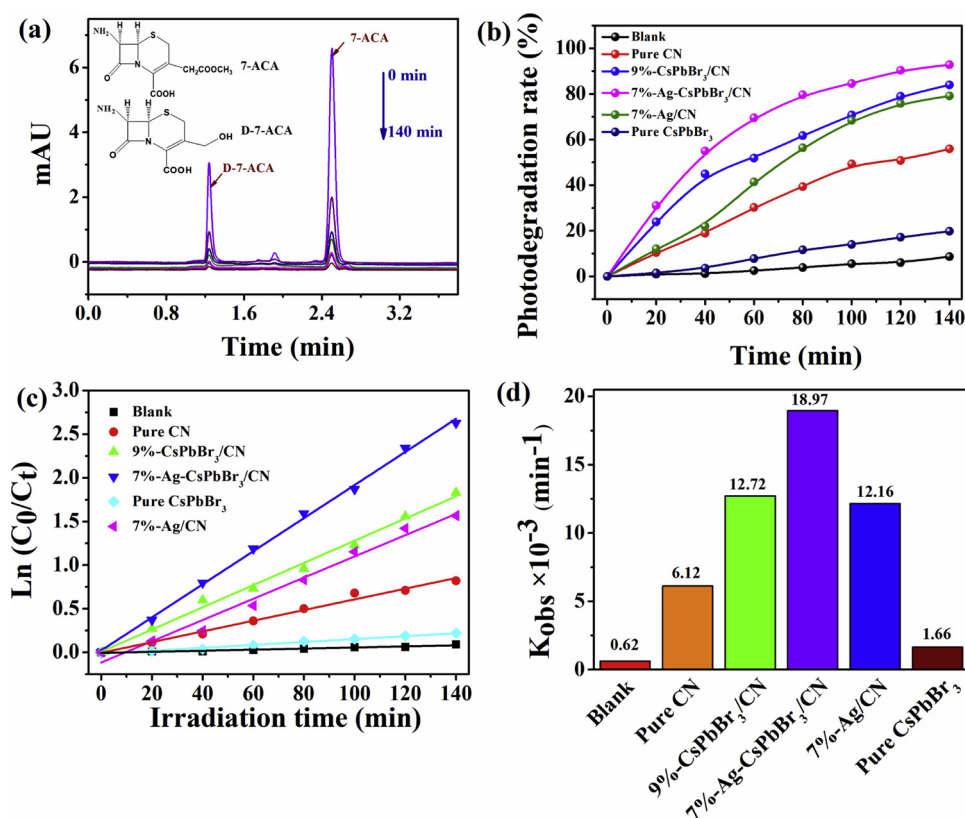
Fig. 5. (a) HPLC chromatograms of 7-ACA, (b) Photocatalytic degradation of 7-ACA with the as-prepared samples, (c) Kinetics fitting with pseudo-first-order, and (d) Photocatalytic degradation rate constant k.

composite depicted the lowest intensity, indicating the excellent charge transportation and separation ability. It is reported that the higher the photocurrent, the better the efficiency of the electrons and holes separation [39]. Fig. 8e displays the transient photocurrent response of the as-prepared samples, and an obvious photocurrent response was observed when the Xe lamp irradiation was turned on, and the electrodes vanished rapidly to their dark current state when the Xe lamp irradiation was turned off, indicating the good reproducibility. The photocurrent of Ag-CsPbBr$_3$/CN composite was significantly higher than CsPbBr$_3$/CN composite and pure CN, indicating more efficient charge transfer. The EIS was employed to test the electro-catalytic activity and to detect the charge transfer processes at solid/electrolyte

interfaces because the EIS was a powerful tool to explore the electrochemical process. It is well known that the smaller the arc radius, the efficiency of charge transfer [4,49]. Te arc radius of 7%-Ag-CsPbBr$_3$/CN composite was smallest, which meant the lower resistance value for electron transfer, indicating an effective charge transportation and separation ability (Fig. 8f).

Therefore, the enhanced photocatalytic activity of the Ag-CsPbBr$_3$/CN composite could be totally attribute to the outstanding adsorbability, the expanding light-harvesting scope, the effective charge transportation and separation ability, as well as the synergistic effects of nano-Ag and CsPbBr$_3$ co-loaded with CN.
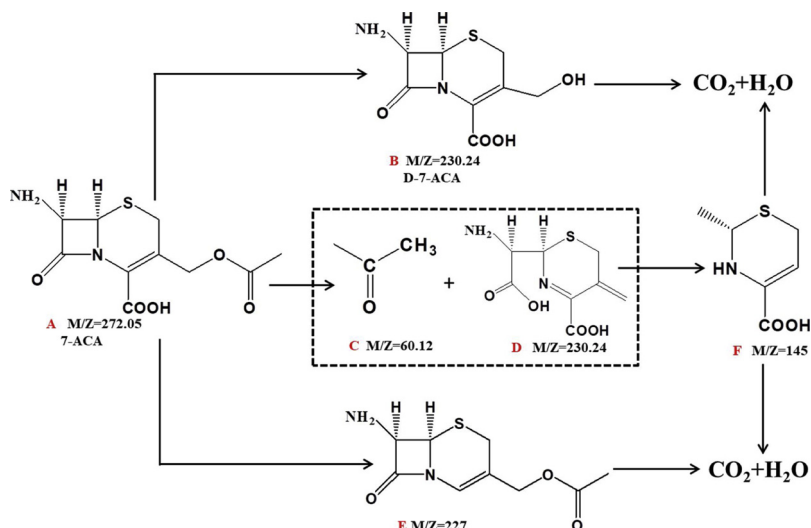

Fig. 6. The predicted products obtained during 7-ACA degradation with 7%- Ag-CsPbBr$_3$/CN composite under visible light irradiation.
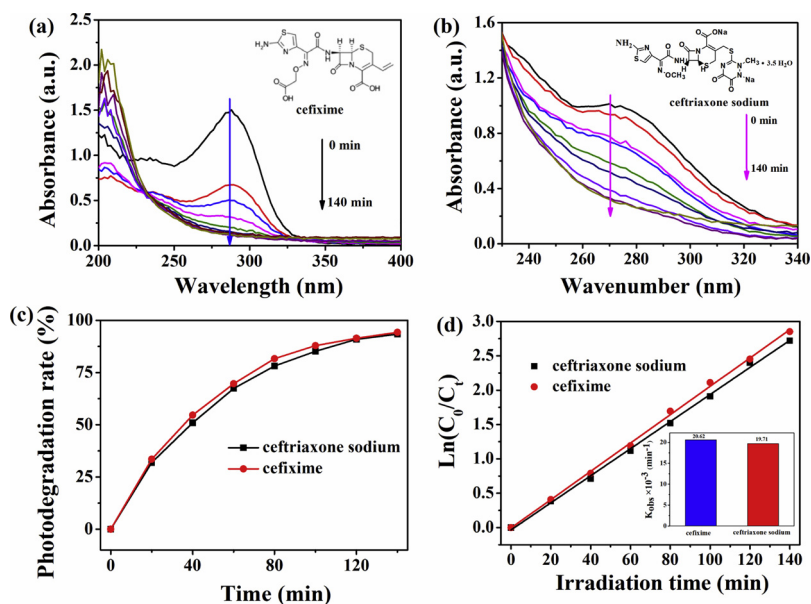
Fig. 7. The variations in (a) cefixime solution absorbance, and (b) ceftriaxone sodium solution absorbance, (c) photocatalytic degradation of cefixime and ceftriaxone sodium with 7%-Ag-CsPbBr$_3$/CN composite, (d) Kinetics fitting with pseudo-first-order and photocatalytic degradation rate constant k.
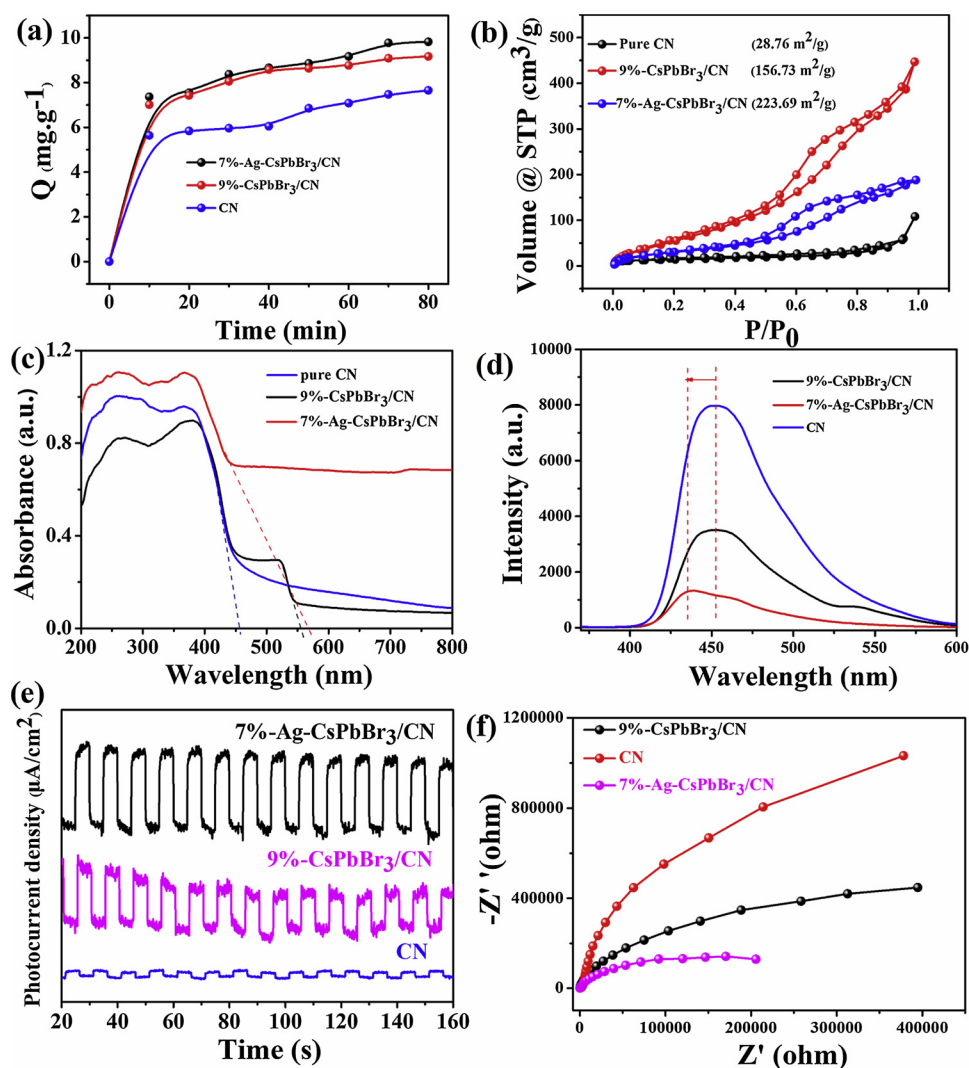

Fig. 8. (a) The adsorbability, (b) Nitrogen adsorption-desorption isotherms, (c) UV-vis diffused absorption spectra, (d) PL spectra, (e) Transient photocurrent response, (f) EIS of the as-prepared samples.
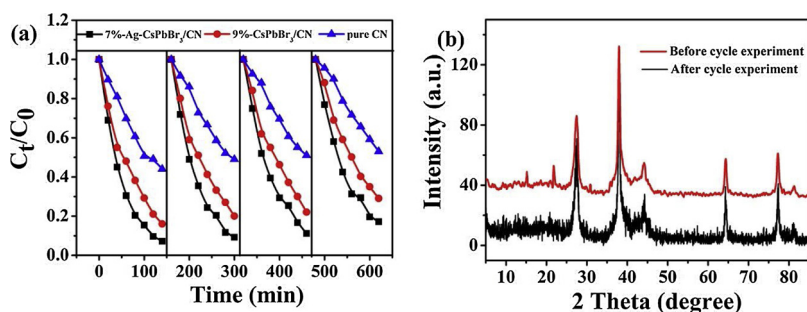
Fig. 9. (a) Cycling experiments, (b) XRD patterns before and after cycle experiment.

3.4. Stability of the as-prepared samples

As the stability of photocatalyst plays an important role in potential application for removing organic pollutant, the recycling experiment runs for 7-ACA degradation under visible light irradiation was employed, and the results were shown in Fig. 9a. The photocatalytic activity of the photocatalyst were effectively maintained except for the degradation rate of Ag-CsPbBr$_3$/CN, CsPbBr$_3$/CN and pure CN decrease from 92.79, 83.96, and 55.96% to 83.19, 71.26 and 47.08% respectively after four cycling reactions. The degradation rates were decreased mainly because of the inevitably loss of the photocatalyst mass during the recycling process.

In order to further evaluation the stability of Ag-CsPbBr$_3$/CN composite system, XRD patterns, XPS spectra, SEM image, EDS and elemental mapping after the recycling experiment were employed, and the results were shown in Fig. 9b, Fig. S3 and Fig. S4. The XRD patterns before and after cycle experiment have similar signals, indicating the stability of the photocatalyst. As shown in Fig. S3, the shape of the Ag-CsPbBr$_3$/CN composite was irregular bulk, C, N, Cs, Pb, Br and Ag elements were found in the EDS spectrum and the elemental mapping. From the full-scan XPS spectra we can see that the C, N, Br, Pb, Cs, O and Ag elements co-exist in the Ag-CsPbBr$_3$/CN composite, and the binding energy of the elements are similar to the composite before cycle experiment (Fig. S4). The results indicated the stability of the Ag-CsPbBr$_3$/CN composite after four recycling experiment.

3.5. Discussion of underlying photocatalytic mechanisms

3.5.1. Detection of reactive species

The reactive-species-trapping experiments were carried out to understand the possible photocatalytic mechanism of the as-prepared samples under visible light irradiation. As shown in Fig. S5, the degradation rate with CN as photocatalyst were significant decreased to 11.22 and 11.34% after addition of P-BQ and K$_2$Cr$_2$O$_7$ quenchers, indicating that ·O$_2$- and e- play major role for pure CN. For Ag-CsPbBr$_3$/CN composite, the dramatically suppressed phenomena were observed by adding EDTA-2Na and IPA scavengers, indicating that h$^+$ and ·OH were the active reactive species, e$^-$ and ·O$_2^-$ were the unimportant species.

NBT methods were used as a detection agent of ·O$_2^-$ radicals to better understand the ·O$_2^-$ radicals formation as the characteristic absorption peak of NBT at 259 nm but the Formanzan precipitate (the reaction product of NBT with ·O$_2^-$) not [39,49,50]. As shown in Fig. 10a, the maximum absorption peaks at 259 nm decreases obviously with irradiation time prolonged, indicating that a great deal of ·O$_2$- radicals were produced from the electrons of pure CN. In contrast, the peaks at 259 nm displayed the negligible decrease with 9%-CsPbBr$_3$/CN (Fig. 10b) and 7%-Ag-CsPbBr$_3$/CN composite (Fig. 10c), suggesting that almost no ·O$_2^-$ radicals were produced, demonstrating the unimportant roles of ·O$_2^-$ radicals in the photocatalytic oxidation reaction, and the results were coincided with BQ trapping experiments in Fig. S5.

Based on the results of reactive-species-trapping experiments, we have found that the 7-ACA degradation mechanism over the CsPbBr$_3$/CN and Ag-CsPbBr$_3$/CN composite related to ·OH attack, larger amount of ·OH radicals, higher are the photocatalytic activities. 7-hydroxycoumarin fluorescent methods were employed to further investigate the formation of ·OH free radicals during the photocatalytic reaction process, for ·OH could react with coumarin to produce luminescent 7-hydroxycoumarin [4,14]. The excitation and emission peaks of 7-hydroxycoumarin were at 390 and 455 nm, respectively. As revealed in Fig. 11a, the maximum fluorescent peaks were turn red shift from 435 to 410 nm under visible light irradiation, and the 7-hydroxycoumarin peaks were not observed, indicating the negligible production of ·OH radicals over the pure CN. Whereas, the maximum fluorescent peaks at 455 nm were discovered in Fig. 11b and c, suggesting the formation of the 7-Hydroxycoumarin. The intensity of 7-Hydroxycoumarin peaks were obviously increased with the irradiation time prolong, indicating the abundant formation of ·OH radicals during the photocatalysis process over 9%-CsPbBr$_3$/CN and 7%-Ag-CsPbBr$_3$/CN composite. From Fig. 11d we can clearly see that 7%-Ag-CsPbBr$_3$/CN composite displayed the biggest fluorescence intensity, suggesting the largest amount of ·OH radicals were formed during the photocatalysis process, illustrating the excellent photocatalytic activity.

3.5.2. Possible photocatalytic mechanism

The Mott-Schottky plots were employed to investigate the flat-band potentials of the as-prepared samples. As shown in Fig. 12, the CsPbBr$_3$/CN and Ag-CsPbBr$_3$/CN composite exhibited the characteristics of n-type semiconductor due to the slope of the linear parts were positive [51]. The flat-band potentials of the 9%-CsPbBr$_3$/CN and 7%-Ag-CsPbBr$_3$/CN composite are approximately −0.49 and −0.30 V versus the saturated calomel electrode (SCE), and are about −0.25, and
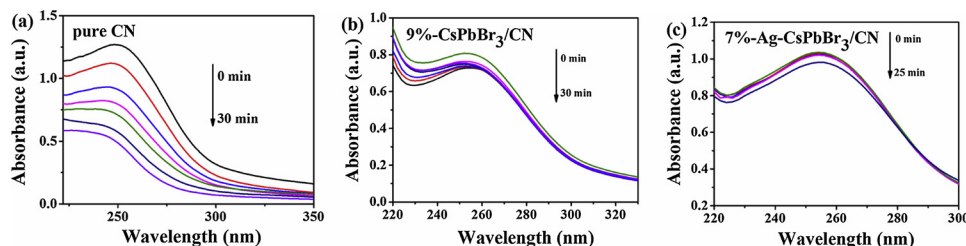

Fig. 10. Spectrum of NBT transformation generated by (a) pure CN, (b) 9%-CsPbBr$_3$/CN, and (c) 7%-Ag-CsPbBr$_3$/CN under visible light irradiation.
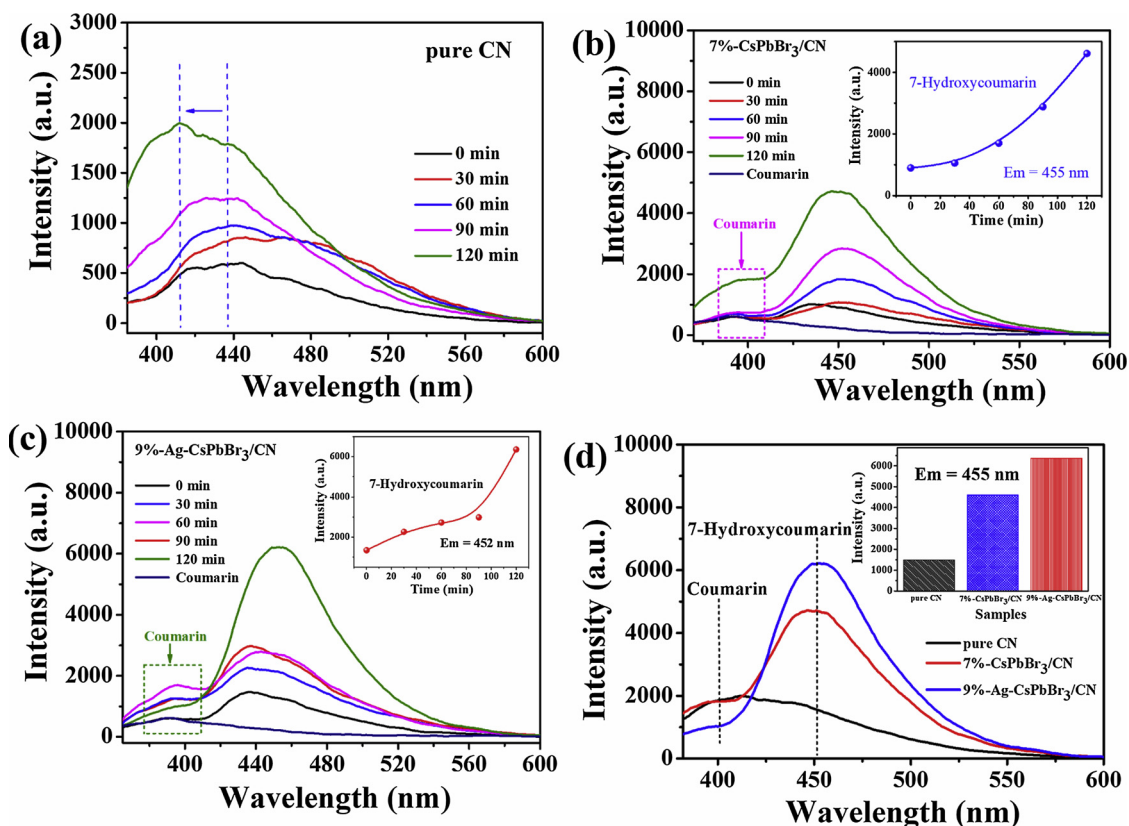
Fig. 11. PL spectra related to the hydroxyl radicals formation under visible-light irradiation with the as-prepared samples. (a) pure CN, (b) 9%-CsPbBr$_3$/CN, (c) 7%-Ag-CsPbBr$_3$/CN, (d) all the as-prepared samples.
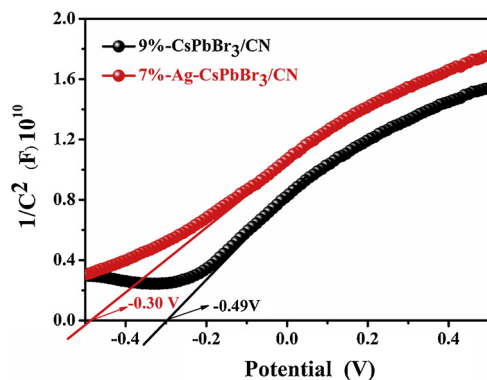

Fig. 12. Mott-schottky plots of the as-prepared samples.

-0.06 eV versus NHE (NHE = SCE + 0.24 V). As the flat-band potentials of the n-type semiconductors are approximately equivalent to the Fermi Levels (Ef) [10], compared with the CsPbBr$_3$/CN, a positive shift of the flat band potential of Ag-CsPbBr$_3$/CN indicates the synergistic effect of Ag, CsPbBr$_3$ and CN, which were beneficial to the transmission of photo-induced carriers [51,52].

The possible mechanism of Ag-CsPbBr$_3$/CN composite responsible for the enhanced photocatalytic activity is elucidated on the basis of the above experimental results, and the schematic illustration is shown in Fig. 13. For the pure CN and CsPbBr$_3$, photo-irradiation first excites electrons from the VB into the CB and leaving holes behind. In the Ag-CsPbBr$_3$/CN composite system, the electrons can be further transferred form VB of CN to Ag in two pathways in direct contact with the Ag or apart from Ag through the mediator CsPbBr$_3$. In the first pathway, as the CB and VB edge potential of pure CN are about -1.33 and 1.40 eV, and the CB and VB edge potential of CsPbBr$_3$ are about -1.13 and 1.1 eV [30,33,34], respectively. The electrons could transfer from the

CB of pure CN to CsPbBr$_3$, and the holes were left in the VB of each semiconductor. As the work function of Ag (4.2 eV) was higher than that of the CsPbBr$_3$ (2.36 eV) [10,36], the electrons could transfer from CsPbBr$_3$ to Ag. Here, CsPbBr$_3$ work as the electron mediator facilitate photo-induced electron transfer from CN to CsPbBr$_3$ and then from CsPbBr$_3$ to Ag enhances the efficiency separation of photo-induced carriers. In the second pathway, the electron could direct transfer from the CB of CN to Ag, facilitating the separation of electrons and holes. In the Ag-CsPbBr$_3$/CN composite system, the reactive species including $\cdot O_2^-$, h$^+$ and $\cdot$OH could attack the cephalosporin antibiotics, and degrade them to CO_2, H_2O and other small molecules, finally degrade to CO_2, H_2O as the degradation time prolong.

4. Conclusions

In summary, the new ternary assembly of Ag-CsPbBr$_3$/CN composite with excellent photocatalytic activity has been firstly synthesized by loading nano-Ag onto the surface of CsPbBr$_3$/CN composite for 7-ACA degradation under visible light irradiation. The enhanced photocatalytic activity of Ag-CsPbBr$_3$/CN composite could be attributed to the excellent adsorbability, the enhanced light-harvesting and reduced charge recombination, as well as the synergistic effects of nano-Ag and CsPbBr$_3$ QDs co-loaded with CN. In addition, the h$^+$ and $\cdot$OH were the active reactive species and the e- and $\cdot$O$_2$- were the unimportant species in 7-ACA degradation process based on the role of reactive species, the NBT transformation, and the 7-hydroxycoumarin fluorescent experiments. The reactive species attack the 7-ACA molecules to degrade which into CO_2, H_2O and other small molecules. The present work may provide a new insight for constructing novel photocatalyst and may have practical applications in the removal of antibiotics.
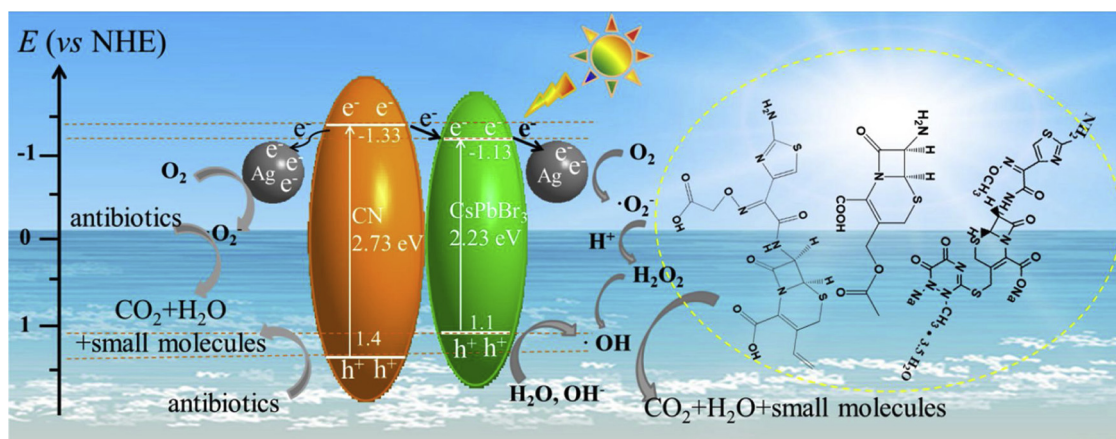
Fig. 13. Possible mechanism diagram for cephalosporin antibiotics degradation with Ag-CsPbBr$_3$/CN composite under visible light irradiation.

Acknowledgments

Appendix A. Supplementary data

Supplementary material related to this article can be found, in the online version, at doi:https://doi.org/10.1016/j.apcatb.2019.01.090.

References

[1] W.Q. Guo, H.S. Zheng, S. Li, J.S. Du, X.C. Feng, R.L. Yin, Q.L. Wu, N.Q. Ren, J.S. Chang, Removal of cephalosporin antibiotics 7-ACA from wastewater during the cultivation of lipid-accumulating microalgae, Bioresour. Technol. 221 (2016) 284–290.

[2] X.H. Wang, Angela Y.C. Lin, Phototransformation of cephalosporin antibiotics in an aqueous environment results in higher toxicity, Environ. Sci. Technol. 46 (2012) 12417–12426.

[3] Y. Zhao, X. Liang, Y. Wang, H. Shi, E. Liu, J. Fan, X. Hu, Degradation and removal of ceftriaxone sodium in aquatic environment with Bi$_2$WO$_6$/g-C$_3$N$_4$ photocatalyst, J. Colloid. Interf. Sci. 523 (2018) 7–17.

[4] Y. Zhao, X. Liang, H. Shi, Y. Wang, Y. Ren, E. Liu, X. Zhang, J. Fan, X. Hu, Photocatalytic activity enhanced by synergistic effects of nano-silver and ZnSe quantum dots co-loaded with bulk g-C$_3$N$_4$ for ceftriaxone sodium degradation in aquatic environment, Chem. Eng. J. 353 (2018) 56–68.

[5] Y. Zhao, Y. Wang, H. Shi, E. Liu, J. Fan, X. Hu, Enhanced photocatalytic activity of ZnSe QDs/g-C$_3$N$_4$ composite for Ceftriaxone sodium degradation under visible light, Mater. Lett. 231 (2018) 150–153.

[6] J. Zhao, Z. Zhao, N. Li, J. Nan, R. Yu, J. Du, Visible-light-driven photocatalytic degradation of ciprofloxacin by a ternary Mn$_2$O$_3$/Mn$_3$O$_4$/MnO$_2$ valence state heterojunction, Chem. Eng. J. 353 (2018) 805–813.

[7] M. Zhu, S. Kin, L. Mao, M. Fujitsuka, J. Zhang, X. Wang, T. Majima, Metal-free photocatalyst for H$_2$ evolution in visible to near-infrared region: black phosphorus/graphitic carbon nitride, J. Am. Chem. Soc. 139 (2017) 13234–13242.

[8] X. Li, T. Wan, J. Qiu, H. Wei, F. Qin, Y. Wang, Y. Liao, Z. Huang, X. Tan, In-situ photocalorimetry-fluorescence spectroscopy studies of RhB photocatalysis over Z-scheme g-C$_3$N$_4$@Ag@Ag$_3$PO$_4$ nanocomposites: a pseudo-zero-order rather than a first-order process, Appl. Catal. B-Environ. 217 (2017) 591–602.

[9] Z. Tong, D. Yang, Z. Li, Y. Nan, F. Ding, Y. Shen, Z. Jiang, Thylakoid-inspired multishell g-C$_3$N$_4$ nanocapsules with enhanced visible-light harvesting and electron transfer properties for high-efficiency photocatalysis, ACS. Nano 11 (2017) 1103–1112.

[10] F. Wang, Y. Wang, Y. Feng, Y. Zeng, Z. Xie, Q. Zhang, Y. Su, P. Chen, Y. Liu, K. Yao, W. Lv, G. Liu, Novel ternary photocatalyst of single atom-dispersed silver and carbon quantum dots co-loaded with ultrathin g-C$_3$N$_4$ for broad spectrum photocatalytic degradation of naproxen, Appl. Catal. B Environ. 221 (2018) 510–520.

[11] L. Ge, C. Han, J. Liu, Novel visible light-induced g-C$_3$N$_4$/Bi$_2$WO$_6$ composite photocatalyst for efficient degradation of methyl orange, Appl. Catal. B Environ. 108–109 (2011) 100–107.

[12] S.K. Cushing, J. Li, F. Meng, T.R. Senty, S. Suri, M. Zhi, M. Li, A.D. Bristow, N. Wu, Photocatalytic activity enhanced by plasmonic resonant energy transfer from metal to semiconductor, J. Am. Chem. Soc. 134 (2012) 15033–15041.

[13] S. Ma, S. Zhan, Y. Jia, Q. Shi, Q. Zhou, Enhanced disinfection application of Ag-modified g-C$_3$N$_4$ composite under visible light, Appl. Catal. B Environ. 186 (2016) 77–87.

[14] A. Zada, Y. Qu, S. Ali, N. Sun, H. Lu, R. Yan, X. Zhang, L. Jing, Improved visible-light activities for degrading pollutants on TiO$_2$/g-C$_3$N$_4$ nanocomposites by decorating SPR Au nanoparticles and 2,4-dichlorophenol decomposition path, J. Hazard. Mater. 342 (2018) 715–723.

[15] Z. Yang, L. Huang, Y. Xie, Z. Lin, Y. Fan, D. Liu, L. Chen, Z. Zhang, X. Wang, Controllable synthesis of Bi$_2$WO$_6$ nanoplate self-assembled hierarchical erythrocyte microspheres via a one-pot hydrothermal reaction with enhanced visible light photocatalytic activity, Appl. Surf. Sci. 403 (2017) 326–334.

[16] S. Kurmar, A. Baruah, S. Tonda, B. Kumar, V. Shanker, B. Sreedhar, Cost-effective and eco-friendly synthesis of novel and stable N-doped ZnO/g-C$_3$N$_4$ core–shell nanoplates with excellent visible-light responsive photocatalysis, Nanoscale. 6 (2014) 4830–4842.

[17] S. Yu, Z.J. Li, X.B. Fan, J.X. Li, F. Zhan, X.B. Li, Y. Tao, C.H. Tung, L.Z. Wu, Vectorial electron transfer for improved hydrogen evolution by mercaptopropionic-acid-regulated CdSe Quantum-Dots-TiO$_2$-Ni(OH)$_2$ assembly, Chemsuschem. 8 (2015) 642–649.

[18] H. Yu, Y. Zhao, C. Zhou, L. Shang, Y. Peng, Y. Cao, L.Z. Wu, C.H. Tung, T. Zhang, Carbon quantum dots/TiO2 composites for efficient photocatalytic hydrogen evolution, J. Mater. Chem. A. 2 (2014) 3344–3351.

[19] K. Wang, G. Zhang, J. Li, Y. Li, X. Wu, 0D/2D Z-scheme heterojunctions of bismuth tantalate quantum dots/ultrathin g-C$_3$N$_4$ nanosheets for highly efficient visible light photocatalytic degradation of antibiotics, Acs. Appl. Mater. Interfaces 9 (2017) 43704–43715.

[20] S. Sarkar, V.K. Ravi, S. Banerjee, G.R. Yettapu, G.B. Markad, A. Nag, P. Mandal, Terahertz spectroscopic probe of hot electron and hole transfer from colloidal CsPbBr$_3$ perovskite nanocrystals, Nano. Lett. 17 (2017) 5402–5407.

[21] J. Song, J. Li, X. Li, L. Xu, Y. Dong, H. Zeng, Quantum dot light-emitting diodes based on inorganic perovskite cesium lead halides (CsPbX$_3$), Adv. Mater. 27 (2015) 7162–7167.

[22] C. Sun, Y. Zhang, C. Ruan, C. Yin, X. Wang, Y. Wang, W.W. Yu, Efficient and stable white leds with silica-coated inorganic perovskite quantum dots, Adv. Mater. 28 (2016) 10088–10094.

[23] Y.F. Xu, M.Z. Yang, B.X. Chen, X.D. Wang, H.Y. Chen, D.B. Kuang, C.Y. Su, A CsPbBr$_3$ Perovskite quantum dot/graphene oxide composite for photocatalytic CO$_2$ reduction, J. Am. Chem. Soc. 139 (2017) 5660–5663.

[24] Z.J. Li, E. Hofman, J. Li, A.H. Davis, C.H. Tung, L.Z. Wu, W. Zheng, Photoelectrochemically active and environmentally stable CsPbBr$_3$/TiO$_2$ core/shell nanocrystals, Adv. Funct. Mater. 28 (2018) 1704288.

[25] S.K. Balakrishnan, P.V. Kamat, Au-CsPbBr$_3$ hybrid architecture: anchoring gold nanoparticles on cubic perovskite nanocrystals, ACS. Energy. Lett. 2 (2017) 88–93.

[26] L. Liu, S. Ouyang, J. Ye, Gold-nanorod-photosensitized titanium dioxide with wide-range visible-light harvesting based on localized surface plasmon resonance, Angew. Chem. Int. Ed. 52 (2013) 6689–6693.

[27] W. Zhang, L. Zhou, H. Deng, Ag modified g-C$_3$N$_4$ composites with enhanced visible-light photocatalytic activity for diclofenac degradation, J. Mol. Catal. A-Chem. 423 (2016) 270–276.

[28] X. Xiao, X. Wei, J. Yang, R. Xiong, C. Pan, J. Shi, Photoreactivity and mechanism of g-C$_3$N$_4$ and Ag Co-Modified Bi$_2$WO$_6$ microsphere under visible light irradiation, Chem. Eng. J. 4 (6) (2016) 3017–3023.

[29] L. Ge, C. Han, J. Liu, Y. Li, Enhanced visible light photocatalytic activity of novel polymeric g-C$_3$N$_4$ loaded with Ag nanoparticles, Appl. Catal. A-Gen 409–410 (2011) 215–222.

[30] G. Gao, Q. Xi, H. Zhou, Y. Zhao, C. Wu, L. Wang, P. Guo, J. Xu, Novel inorganic perovskite quantum dots for photocatalysis, Nanoscale. 9 (2017) 12032–12038.

[31] Y.X. Zhang, H.Y. Wang, Z.Y. Zhang, Y. Zhang, C. Sun, Y.Y. Yue, L. Wang, Q.D. Chen, H.B. Sun, Photoluminescence quenching of inorganic cesium lead halides

perovskite quantum dots (CsPbX₃) by electron/hole acceptor, Phys. Chem. Chem. Phys. 19 (2017) 1920–1926.

[32] J.B. Hoff ;man, A.L. Schleper, P.V. Kamat, Transformation of sintered CsPbBr₃ nanocrystals to cubic CsPbI₃ and gradient CsPbBrₓI₃₋ₓ through Halide exchange, J. Am. Chem. Soc. 138 (2016) 8603–8611.

[33] P. Luo, Y. Zhou, S. Zhou, Y. Lu, C. Xu, W. Xia, L. Sun, Fast anion-exchange from CsPbI₃ to CsPbBr₃ via Br₂-vapor-assisted.deposition for air-stable all-inorganic perovskite solar cells, Chem. Eng. J. 343 (2018) 146–154.

[34] M. Ou, W. Tu, S. Yin, W. Xing, S. Wu, H. Wang, S. Wan, Q. Zhong, R. Xu, Amino-assisted anchoring of CsPbBr₃ perovskite quantum dots on porous g-C₃N₄ for enhanced photocatalytic CO₂ reduction, Angew. Chem. Int. Ed. 57 (2018) 13570–13574.

[35] R. Wang, X. Kong, W. Zhang, W. Zhu, L. Huang, J. Wang, X. Zhang, X. Liu, N. Hu, Y. Suo, J. Wang, Mechanism insight into rapid photocatalytic disinfection of salmonella based on vanadate QDs-interspersed g-C₃N₄ heterostructures, Appl. Catal. B-Environ. 225 (2018) 228–237.

[36] J. Sun, Y. Guo, Y. Wang, D. Cao, S. Tian, K. Xiao, R. Mao, X. Zhao, H₂O₂ assisted photoelectrocatalytic degradation of diclofenac sodium at g-C₃N₄/BiVO₄ photoanode under visible light irradiation, Chem. Eng. J. 332 (2018) 312–320.

[37] O.F. Carceller, M.J. Muñoz-Batista, M. Fernández-García, A. Kubacka, Interface effects in sunlight-driven Ag/g-C₃N₄ composite catalysts: study of the toluene photodegradation quantum efficiency, ACS. Appl. Mater. Interfaces 8 (2016) 2617–2627.

[38] Y. Ma, J. Li, E. Liu, J. Wan, X. Hu, J. Fan, High efficiency for H₂ evolution and NO removal over the Ag nanoparticles bridged g-C₃N₄ and WS₂ heterojunction photocatalysts, Appl. Catal. B-Environ. 219 (2017) 467–478.

[39] J. Wan, X. Du, E. Liu, Y. Hu, J. Fan, X. Hu, Z-scheme visible-light-driven Ag₃PO₄ nanoparticle@MoS₂ quantum dot/few-layered MoS₂ nanosheet heterostructures with high efficiency and stability for photocatalytic selective oxidation, J. Catal. 345 (2017) 281–294.

[40] Y. Bu, Z. Chen, W. Li, Using electrochemical methods to study the promotion mechanism ofthe photoelectric conversion performance of Ag-modified mesoporous g-C₃N₄ heterojunction material, Appl. Catal. B Environ. 144 (2014) 622–630.

[41] X. Wu, C. Lu, J. Liu, S. Song, C. Sun, Constructing efficient solar light photocatalytic system with Ag-introduced carbon nitride for organic pollutant elimination, Appl. Catal. B Environ. 217 (2017) 232–240.

[42] X. Li, Y. Wu, S. Zhang, B. Cai, Y. Gu, J. Song, H. Zeng, CsPbX₃ quantum dots for lighting and displays: room-temperature synthesis, photoluminescence superiorities, underlying origins and white light-emitting diodes, Adv. Funct. Mater. 26 (2016) 2435–2445.

[43] S. Liu, Y. Luo, M. He, X. Liang, W. Xiang, Novel CsPbI3 QDs glass with chemical stability and optical properties, J. Eur. Ceram. Soc. 38 (2018) 1998–2004.

[44] J. Hou, S. Cao, Y. Wu, Z. Gao, F. Liang, Y. Sun, Z. Lin, L. Sun, Inorganic colloidal perovskite quantum dots for robust solar CO₂ reduction, Chem. Eur. J. 23 (2017) 9481–9485.

[45] Z. Li, L. Zhu, W. Wu, S. Wang, L. Qiang, Highly efficient photocatalysis toward tetracycline under simulatedsolar-light by Ag⁺-CDs-Bi₂WO₆: synergistic effects of silver ions andcarbon dots, Appl. Catal. B-Environ. 192 (2016) 277–285.

[46] N. Tian, Y. Zhang, X. Li, K. Xiao, X. Du, F. Dong, G.I.N. Waterhouse, T. Zhang, H. Huang, Precursor-reforming protocol to 3D mesoporous g-C₃N₄ established by ultrathin self-doped nanosheets for superior hydrogen evolution, Nano. Energy 38 (2017) 72–81.

[47] K. Maeda, X. Wang, Y. Nishihara, D. Lu, M. Antonietti, K. Domen, Photocatalytic activities of graphitic carbon nitride powder for water reduction and oxidation under visible light, J. Phys. Chem. C. 113 (2009) 4940–4947.

[48] Y. Chen, B. Wang, S. Lin, Y. Zhang, X. Wang, Activation of n → pi* transitions in two-dimensional conjugated polymers for visible light photocatalysis, J. Phys. Chem. C. 118 (2014) 29981–29989.

[49] N. Tian, H. Huang, Y. He, Y. Guo, T. Zhang, Y. Zhang, Mediator-free direct Z-scheme photocatalytic system: BiVO₄/g-C₃N₄ organic-inorganic hybrid photocatalyst with highly efficient visible-lightinduced photocatalytic activity, Dalton. T. 44 (2015) 4297–4307.

[50] H. Zhai, T. Yan, P. Wang, Y. Yu, W. Li, J. You, B. Huang, Effect of chemical etching by ammonia solution on the microstructure and photocatalytic activity of Ag₃PO₄ photocatalyst, Appl. Catal. A Gen. 528 (2016) 104–112.

[51] T. Xu, L. Zhang, H. Cheng, Y. Zhu, Significantly enhanced photocatalytic performance of ZnO via grapheme hybridization and the mechanism study, Appl. Catal. B Environ. 101 (2011) 382–387.

[52] Y. Bai, L. Ye, T. Chen, L. Wang, X. Shi, X. Zhang, D. Chen, Facet-dependent photocatalytic N₂ fixation of bismuth-rich Bi₅O₇I nanosheets, ACS. Appl. Mater. Interfaces 8 (2016) 27661–27668.